Universidad de La Laguna

DESIGN OF SUB-WAVELENGTH TRANSMISSION GRATINGS FABRICATED BY MEANS OF 3D FEMTOSECOND NANOLITHOGRAPHY

Master in Nanoscience and Molecular Nanotechnology

Author: Alfredo CASASNOVAS MELIÁN

Academic tutor: DR. Airán RÓDENAS SEGUÍ

Academic year: 2020-2021

ABSTRACT

This Master's Thesis aims to make a study about transmission subwavelength diffraction gratings in volume, giving an explanation about the diffraction phenomena, conditions that must fulfil them and an overview about the current situation. Furthermore, simulation results will be exposed applying different geometries and light conditions and, a setup for their fabrication is going to be discussed.

ACKNOWLEDGEMENTS

I am very appreciated to Omar Enrique de Varona Ortega and Franzette Paz Buclatin for helping me on doing my thesis.

TABLE OF CONTENTS

LIST OF SYMBOLS AND ABBREVIATIONS

	Symbol	Long name	Symbol	Long name
Setup acronyms	Pump	Pump laser	n_c	Refractive index of the cladding
	Ti:Sa	Titanium Sapphire laser	n_H	Refractive index of the higher material
	M	Mirror with dielectric antireflection coating	n_L	Refractive index of the lower material
	$\lambda/2, HW$	Half waveplate	n_s	Refractive index of the substrate
	S	Shutter	n_{YAG}	Refractive index of YAG
	PP	Pulse picker	NIR	Near infrared
	BE	Beam expander	OPL	Optical path length
	$\lambda/4, QW$	Quarter waveplate	P_{avg}	Average power
	L	Microscopy objective	P_{peak}	Peak power
	DM	Dichroic mirror	P_{in}	Input power
	C	Collimator	$P_{out}^{(\mathrm{avg})}$	Average output power
	CCD	Charge couple device	$P_{PP}^{(\mathrm{avg})}$	Average pulse picker power
	LED	Light emitting diode	R^2	Pearson coefficient
	PC	Personal computer	RCWA	Rigorous coupled wave analysis
	3DLW	3D laser writing	SPL	Scanning probe lithography
	$\mathrm{A_{rms}}$	Root mean square amperes	TBP	Time bandwidth product
	c	Light speed	TE	Transverse electric mode
	CPA	Chirped pulse amplification	TM	Transverse magnetic mode
	DC	Duty cycle	UV	Ultraviolet
	DE_m	m$^{\mathrm{th}}$ order diffraction efficiency	V	Vertical polarization field
	$DE_m^{(\max)}$	m$^{\mathrm{th}}$ order maximum diffraction efficiency	VDC	Voltage direct current
	EBL	Electron beam lithography	W	Width
	E_P	Pulse energy	YAG	Yttrium aluminium garnet
	FF	Filling Factor	θ	Angle measured from the X axis in the YZ plane
	fs	Femtosecond	Λ	Pitch/ grating period
	H	Horizontal polarization field	λ	Wavelength
	H	Height	λ_0	Wavelength in vacuum
	HV	High voltage source	λ_c	Barycentre
	I	Intensity	$\Delta\lambda$	Bandwidth
	$\vec{k}$	Wave vector	ν	Frequency
	KTP	Potassium titanyl phosphate crystal	ν_{PP}	Pulse repetition rate (for the pulse picker)
	m	Diffraction order	τ	Pulse duration
	n_{air}	Refractive index of air	τ_{PP}	Pulse width (for the pulse picker)
	n_{avg}	Average refractive index	φ	Angle measured from the Z axis in the XZ plane

CHAPTER 1. INTRODUCTION

1.1 Background and motivation

Since Young's and Fraunhofer's light splitting studies on primitive diffraction gratings using silk fabric pieces, around the 18th century [Loewen and Popov 1997], this kind of diffraction optical elements (DOE) [Hazra 1999] have evolved up to our days thanks to the emergence of new technologies and fabrication processes. Even if nowadays they are used for the same purposes that were thought of from the start, new applications are sought since these first steps. According to its operation principle, when light falls upon over a periodic structure with a well-defined geometry and certain dimensions, it will be able to split and scatter light into several orders, both in transmission and reflection, at different angles and frequencies. This powerful fundamental property of gratings and structured optical media will be discussed in more detail in Chapter 2.

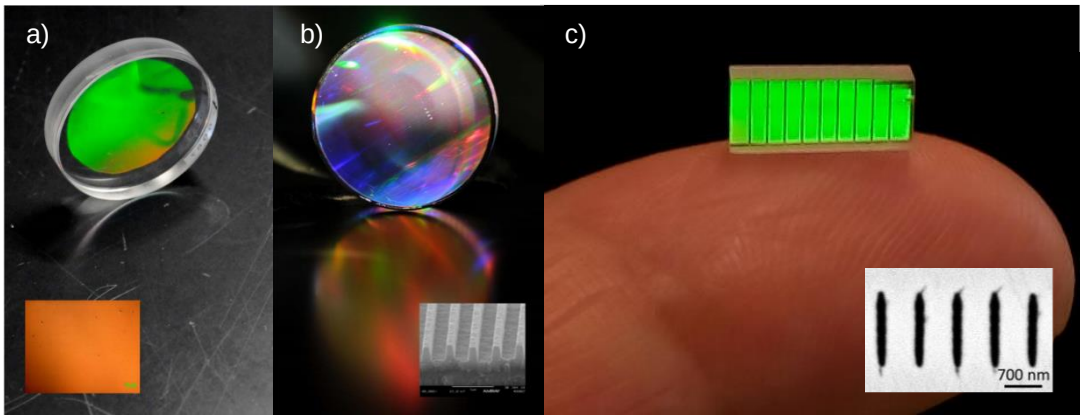

Figure 1-1. Different types of diffraction grating: **a)** a volume grating made by dichromatic gelatine, used in transmission (inset, optical microscope image); **b)** a surface relief grating made by multilayer dielectric films, used in reflection (inset, electronic microscopy image of the grating). Both taken from [Bonod and Newport 2016]. **c)** The subject of this research work: a new kind of grating made inside a YAG crystal by means of fs-pulse 3D laser writing (3DLW) by Dr. A. Ródenas (inset, SEM of the air pores composing the embedded grating).

Presently, there exist a large number of types of gratings, classified depending on either their working principle (reflection or transmission), the materials design of the full grating, and the lithographic fabrication methods. Some examples are given in Fig. 1-1. Gratings are in general optimized to either reflect or transmit diffracted light, and the ways in which each type can be fabricated and designed are numerous, as it is depicted in Fig. 1-2. On the one hand, gratings can be composed by a "sandwich" of different deposited dielectric materials (Fig. 1-1b), by only metallic materials, or by a mixture of both dielectric and metallic layers. Materials can be soft, as with a polymer (Fig. 1-1a) [Bonod and Newport 2016] or hard crystalline materials; these last ones can be used in volume diffraction gratings (Fig. 1-1c) by a recently discovered new method of femtosecond-pulse (fs-pulse) direct laser writing [Ródenas 2018], which is the starting point of this research work.

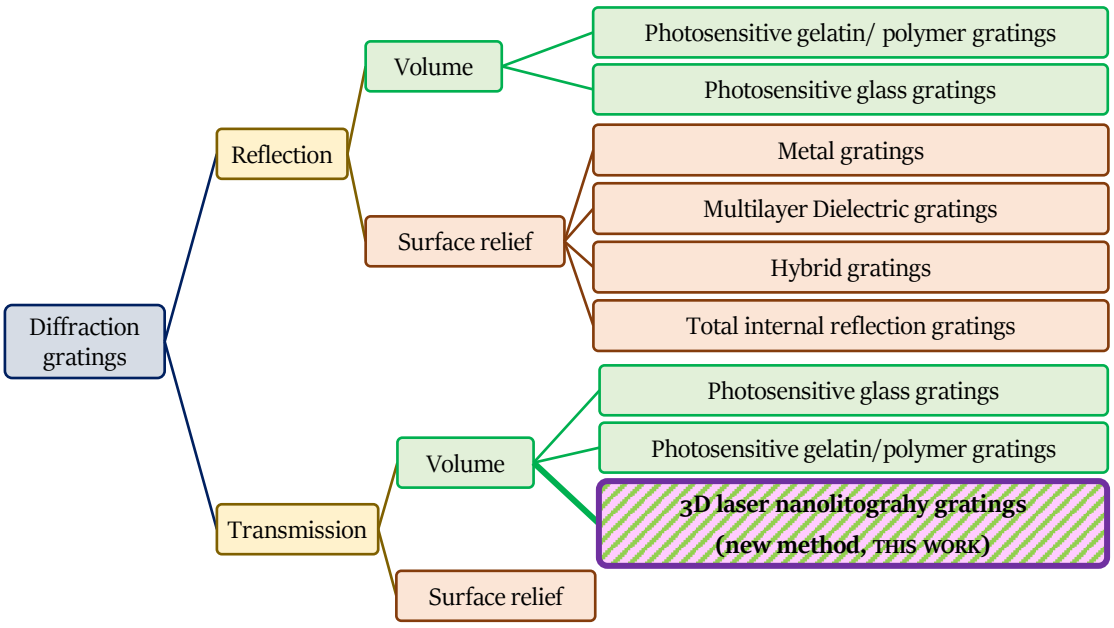

Figure 1-2. Classification of different diffraction gratings most used in optical spectroscopy [Bonod and Newport 2016]. The violet square (with letters in bold) is referred to the kind of diffraction gratings that are going to present in this memory.

Another important aspect that must be taken into account is that surface relief gratings have a much lower damage threshold than volume ones, or in other words, they can be irreversibly damaged more easily than volume ones. The reason for this is that photo-modification and ablation occur more easily at surface defects than within the volume of a transparent material. When irreversible damage occurs, diffraction patterns are destroyed, removing the grating or melting the material, introducing other defects as bubbles, craters, among others. Shown in Fig. 1-3 are some examples [Bonod and Newport 2016], [Manenkov 1974]. In contrast, when volume diffraction gratings are used, they usually have a larger laser damage threshold. In particular, this work will be focused on sub-wavelength gratings inside the volume of hard optical crystals (YAG), a type of transmission diffraction grating where diffractive elements are embedded in a crystal bulk, conferring larger damage thresholds. Thermal damage mechanisms due to the interaction between photo-excited electrons in the conduction band and laser light can occur, but they vary depending on the pulse duration scale, its energy and frequency [Carr et al. 2015].

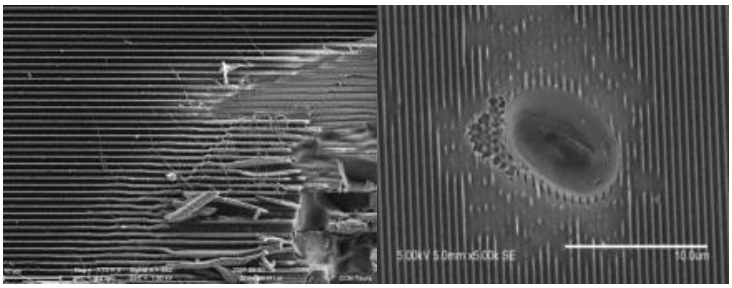

Figure 1-3. SEM images of damaged surface relief transmission gratings after shined with a high intensity laser source [Carr et al. 2015].

Regarding applications, gratings are employed in a myriad of uses [Popov 2012], but only a few of them will be presented. They can be found in every spectroscopy laboratory, for acquire spectra of samples. Moreover, in astronomy, for analysing poor star light. Optical filters are also an important usage, to enhance a certain order, dimming the rest, studied by the 0^{th} order diffraction (ZOD) imaging. Beam steering is a really interesting method in which, taking advantage of diffraction gratings with a particular configuration can modify the light path in a desired way.

Another important application of gratings is the chirped pulse amplification (CPA) technology. This technique was described in Donna Strickland's very first scientific paper [Strickland 1985], and it led to her 2018 Nobel Prize in Physics. The technique allows to amplify the intensity of ultra-short laser pulses. Referring to Fig. 1-4, in step 1, a very short light pulse is stretched using a set of diffraction gratings, to reduce its peak power and avoid damaging optical materials. This in-time-domain broadened pulse comes through an amplifier (step 2), which allows to obtain higher energy pulses (step 3). Compressing back the pulse, one can obtain a high energy pulse within a shorter pulse duration envelope, i.e. a high intensity pulse (step 4) [Rochester 2021].

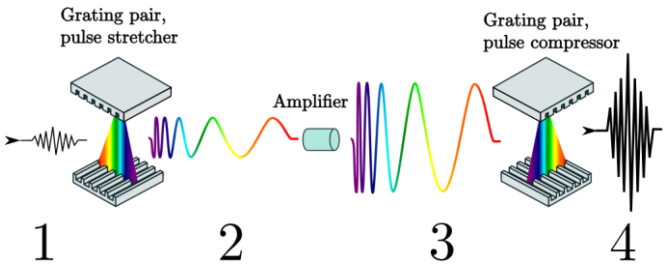

Figure 1-4. Sketch of the chirped-pulse amplification technique. 1^{st} step has an initial short pulse, stretched in 2^{nd} step, amplified in 3^{rd} step, and finally recovering the short pulse in time domain, but much more intense in 4^{th} step.

In summary, there is a need to fabricate new types of diffraction gratings, but also, they must be resistant and very high quality to avoid distortions of the beam profile. In some cases, such as for high power laser applications, they have to be made of sufficiently resistant materials that can overcome extreme conditions without damaging, exhibiting good diffractive properties according to the design, expecting low loses and, they should also be relatively affordable and fast to fabricate, having good manufacturing throughputs.

1.2 Thesis scope

The scope of this master thesis is to present all the information with the purpose of fabricating diffraction gratings and, in particular, about subwavelength diffraction gratings. The work structure is divided in five different chapters, starting with this first one, in which is given a first approximation to the topic. In Chapter 2, a theoretical introduction to diffraction gratings is introduced, and in more detail, about subwavelength gratings. In addition to this, a section about the main 3D fabrication methods for transmission gratings is presented, giving a state-of-the-art overview, and in particular the femtosecond laser writing, technique that is based on this work. Moreover, there is a review about simulation methods

which have been employed with the purpose of designing new transmission diffraction gratings, using two different computer software simulators. After that, the methodology that will be followed to design these own diffraction gratings is explained.

Once the fundamentals are explained, in Chapter 3, numerical simulations were made, exploring the best geometries and ratios, and comparing results given by different publications. In Chapter 4, there is presented an overview of this work, as well as a discussion about the future possibilities to do in the field of subwavelength gratings. Finally, in Appendix, the setup that has been preparing in the laboratory is introduced, presenting a general sketch, with a study of different elements which are used in this setup.

1.3 References

[Loewen and Popov 1997] Loewen E.G. and Popov E. (1997). *Diffraction gratings and applications*. Marcel Dekker Inc.

[Bonod and Neauport 2016] Bonod N. and Neauport J. (2016). Diffraction gratings: from principles to applications in highly-intensity lasers. *Advances in Optics and Photonics*, **8**(1), pp. 1-44.

[Hazra 1999] Hazra L.N. (1999). *Diffractive optical elements: past, present, and future.* Proceedings of SPIE.

[Manenkov 1974] Manenkov A. A. (1974). Fundamental mechanisms of laser-induced damage in optical materials: today's state of understanding and problems. *Optical Engineering*, **53**(1), pp. 010901-1 - 010901-7.

[Carr et al. 2015] Alessi D.A., Carr W., Hackel R.P, Negres R.A., Stanion K., Fair J.E., Cross D.A., Nissen J., Luthi R., Guss G., Britten J.A., Gourdin W.H. and Haefner C. (2015). Picosecond laser damage performance assessment of multilayer dielectric gratings in vacuum. *Optic Express*, **23**(12), pp. 15532-15544.

[Ródenas 2018] Ródenas A., (2018). *3D Laser Nanolithography of Crystals.* [PowerPoint presentation].

[Rumpf 2020] Rumpf R., (2020). *Subwavelength gratings.* [PowerPoint presentation]. University of Texas at El Paso (UTEP).

[Rochester 2021] University of Rochester, (visited at 2021). *Chirped-Pulse Amplification*.

[Strickland 1985] Strickland D. and Mourou G., (1985). Compression of Amplified Chirped Optical Pulses. *Opt. Commun.*, **56** 3219-221

[Popov 2012] Popov E., (2012). *Introduction to Diffraction Gratings: Summary of applications*. Institut Fresnel, CNRS, Université d'Aix-Marseille.

CHAPTER 2. SUBWAVELENGTH GRATINGS

2.1 Introduction to diffraction gratings

A general scheme on the light diffraction process on a perfectly periodical grating can be found in Fig. 2-1 (left). The simplest case corresponds to a finite structure with a binary pattern that repeats in a unique dimension, being able to disperse an incident plane wave (with wave vector $\vec{k}_i$ represented in red), as a sum of plane waves, which are the different diffraction orders, by transmission (wave vector $\vec{k}_t$ in purple) or reflection (wave vector $\vec{k}_r$ in green).

By using the grating equation (Eqs. (2-1) and (2-2)) the propagation directions of these orders can be predicted, both in reflection and transmission regimes, respectively [Erdogan 2021], [Wolf and Born 1980]. No information is however obtained, on the relative intensities of each order.

$$n_r \sin(\theta_{r,m}) = n_i \sin(\theta_i) + m\frac{\lambda_0}{\Lambda} \tag{2-1}$$

$$n_t \sin(\theta_{t,m}) = n_i \sin(\theta_i) + m\frac{\lambda_0}{\Lambda} \tag{2-2}$$

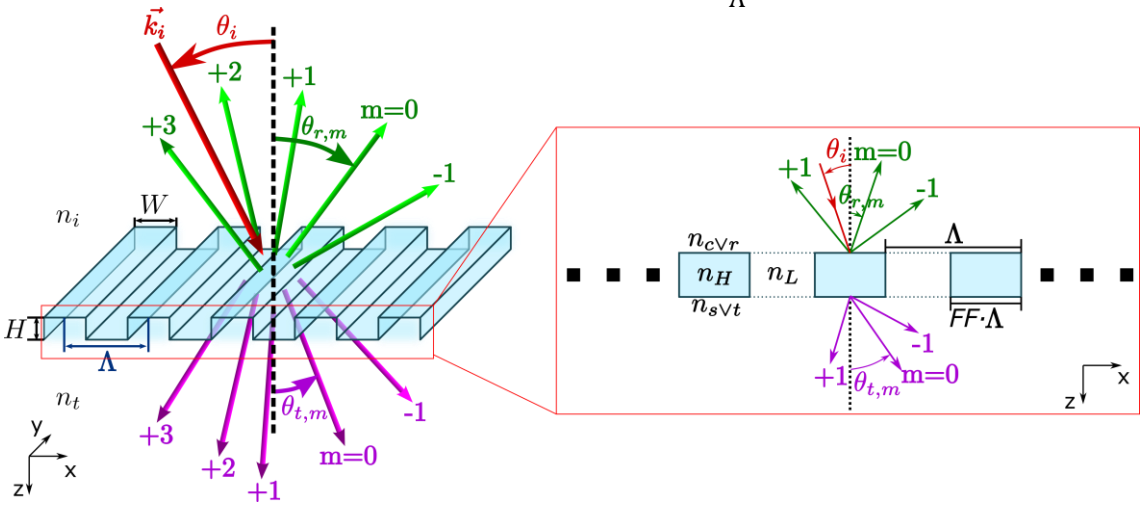

Figure 2-1. General sketch of a diffraction grating with a period Λ, width *W*, height *H*, and transmitted light refractive index n_t, shining a light source at an angle θ_i and wavelength λ_0, coming from a medium with an incident n_i refractive index, and diffracted in several orders, given by the letter *m*, in the reflection regime (in green), with an angle $\theta_{r,m}$ and transmission regime (in purple), $\theta_{r,m}$, for each order. Also, angles are positive as they are shown. Sketch of a simple cross section of a diffraction grating, indicating their refractive indices,

As it can be seen, the grating structure, its composition and environment play an important role, where the incident, n_i, reflected, n_r, and transmitted, n_t refractive indices, as well as, as a general case, all refractive indices of those materials that is made the grating; λ_0 as the incident wavelength light source in vacuum; the grating period, also called pitch Λ, or dg; the grating thickness along the light propagation *H*, the incident light angle θ_i, and $\theta_{r,m}, \theta_{t,m}$ as the reflected and transmitted angles for a certain order $m \in \mathbb{Z}$, respectively (angle convention). The result of these equations is calculated considering the difference of two optical path lengths (OPL) separated by a period, Λ. This equation can be used on any diffraction

grating although, there are some parameters unable to be predicted by this equation, like the light intensity of each order, or polarization phenomena. There are several ways to obtain this equation, so different results can be found in literature [Shimadzu 2021].

Going further in the discussion of refractive indices, the most general (and simple) case is a device that can be summarized as it is presented in Fig. 2-1 (right). A diffraction pattern, composed by a high refractive index, n_H; and a low refractive index region, n_L, regions, is surrounded (sandwiched) by an upper cover, n_c, and a substrate, n_s. In addition, the grating region can be described using the grating period Λ and the grating filling factor, FF, representing the ratio between the width of the higher (or lower) refractive index with respect to the pitch [Wang et al. 2009]. Then, equivalent notation is: $n_i = n_r = n_c$, and $n_t = n_s$.

In grating design, choosing a particular pitch Λ is fundamental. According to this value, there will be a cut-off on diffracted orders, decreasing its number both in transmission and reflection regimes as pitch is reduced. Introducing the effective refractive index in the grating, n_{avg}, given in Eq. (2-3) and, using the scalar grating equation, Eqs. (2-1) and (2-2), order cut-off can be predicted, happening at the condition $|\sin(\theta_m)| > 1$, so that the number of different orders can be predicted. This average refractive index is only a first order approximation, only valid in the subwavelength regime for which the grating period is smaller than the wavelength [Halir et al. 2014].

$$n_{avg} = \sqrt{n_H^2 f + n_L^2 (1 - f)} \tag{2-3}$$

In consequence, four different qualitative grating behaviours can be expected, depending on the relative magnitudes of the light wavelengths (incident and transmitted) against the period of the grating [Rumpf 2020]. This general behaviour is shown in Fig. 2-2.

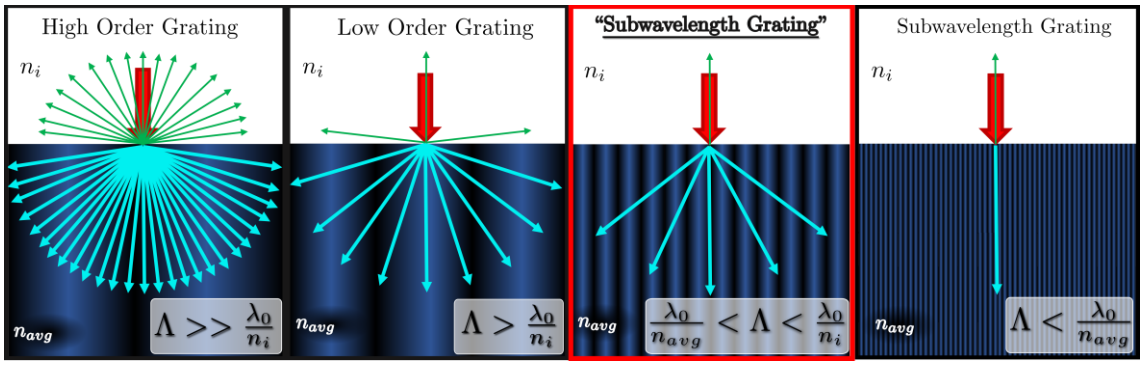

Figure 2-2. General diffraction processes. Remarked, in red, the thesis study field, of "subwavelength" diffraction gratings (considering that $n_{avg} > n_i$). In this case, $n_i = n_r = n_c$.

As shown in Fig. 2-2, if the grating period (Λ) is much larger than the wavelength in the incident medium, i.e., $\Lambda \gg \lambda_0/n_i$, a high order grating is provided, and then a great number of diffracted orders appear in transmission and reflection. Reducing it a bit, a low order grating is obtained. These types of gratings are standard for applications as spectroscopy, where optimal dispersion of light is required, at the cost of losing power at other diffraction orders which are not exploited [Palmer 2020].

A different case arises when the grating period becomes of the order of the wavelength size ($\lambda_0/n_{avg} < \Lambda < \lambda_0/n_i$), becomes in fact, a 1D photonic crystal structure, with the period Λ smaller than the vacuum wavelength λ_0 ("subwavelength gratings") [Ródenas et al. 2019]. In this case, gratings can be designed to have zero reflection (very beneficial for low loss laser applications), as well as having only an order of diffraction which will therefore carry all the incident laser power, something impossible with large period gratings. Beyond this region, if the pitch is much smaller than the lower limit, $\Lambda < \lambda_0/n_{avg}$, then the 0th order is only propagated, the grating is acting as a metamaterial which does not diffract the light [Magnusson 2007].

Another key aspect to keep into account is the case in which the incident angle θ_i coincides with the diffracted angle in reflection regime for the order m (i.e., they are collinear). Then, the system is working under the Littrow configuration or Littrow mounting, sketch in Fig. 2-3. The mathematical expression is achieved by forcing $\theta_{Litt} = \theta_i = -\theta_{r,m}$ in Eq. (2-1), presented in Eq. (2-4):

$$\theta_{Litt} = \text{asin}\left(-m\frac{\lambda_0}{2\Lambda n_i}\right) \tag{2-4}$$

with n_i the incident refractive index; λ_0 the incident wavelength and the pitch Λ. For the order $m = -1$, it can be obtained this angle relation $\theta_i = -\theta_{r,-1} = -\theta_{t,-1}$ [Erdogan 2021].

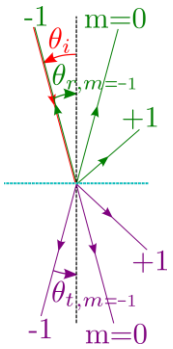

Figure 2-3. Sketch for a diffraction grating being illuminated under Littrow configuration. Incident beam (in red) is dispersed in several orders in reflection (green) and transmission (purple).

Furthermore, another interesting characteristic to take into account when dealing with diffraction gratings is light polarization. Remembering that an electromagnetic field has its amplitude oscillating in a certain direction and, in waveguide propagation there are two main transverse polarized [Palmer 2020]. If the electric component of light is parallel to the diffraction grating, TE mode is propagating through; and, when is the magnetic component, then it is a TM mode (then the electric component is perpendicular to the grating grooves). These modes will be related with the reflectivity and transmission diffraction efficiencies coefficients. As stated above, Eqs. (2-1) and (2-2) do not say anything about the diffracted light intensity. Considering the power of light on each diffracted order compared with the incident power, diffraction efficiency of order m can be defined, given by the ratio of the optical power that results from the diffracted order m respect the incident one: $DE_m = P_m/P_i$. This variable can be used both in transmission and reflection and there are several analytical approximations for this parameter, but they are obtained for particular grating configurations so, in general, it is calculated via computer simulations. The diffraction

efficiency will be a clue parameter, whose main objective will be to try to optimize throughout this Master's work, withing the numerical simulation works.

Combining all of that, as an application example, when a diffraction grating has to be designed for high-power ultrashort pulse chirped pulse amplification CPA (explained in chapter 1), where lowest losses are needed to have on each diffraction grating, work will therefore have to be done under a Littrow configuration, in a first order ($m = -1$). This occurs fulfilling the condition $\lambda/2 < \Lambda < 3\lambda/2n$, being possible to theoretically achieve the 100% of diffraction efficiency for the -1st order, i.e., $DE_{-1}^{(\max)} = 1$ [Clausnitzer et al. 2008], [Bonod and Neauport 2016].

2.2 Fabrication methods for transmission gratings

2.2.1 State of the art

As in the first chapter was introduced, diffraction gratings have evolved greatly after its first steps in 18th century, having different technologies available nowadays. The first modern gratings were made by mechanical processes [Michelson 1915] but, in the 60s, thanks to laser sources and Cotton experiments in the early 20th century, holographic gratings were manufactured, process used up to the present day. It consists in the application of an interference pattern, created by imposing two coherent beams, over a photosensitive layer (like polymers as SU8 or a mixture of diazoquinone and Novolak) which is coated on a substrate (usually fused silica or quartz), resulting in a sinusoidal modulated pattern. After that, the uncured material is removed etching it, by a wet or dry etching. This process must be done in clean, quiet conditions, to avoid undesired scattering defects, that creates ghost patterns in the grating [Cui 2005]. According to the lithographic process, it depends on the optical setup that is managed and, in consequence, its resolution. In the 2000s, scanning beam holography was developed to obtain even better resolutions. Moreover, other techniques that use EBL, or SPL, among others, have been developing in the last decades, however, there are several restrictions in sizes, time, and costs [Bonod and Neauport 2016].

Besides these gratings are used as volume gratings, in which the diffraction occurs by this pattern in volume, surface relief gratings are also made by this technique, only when appears a large index contrast (at least 0.5) between the regions which are illuminated and not. Not only polymers can be used, but also metals like gold is widely used, because it is necessary applying a cladding to protect it. Metallic films are sputtered or evaporated on the profile [Bonod and Neauport 2016].

2.2.2 3D femtosecond-pulse laser nanolithography

The femtosecond-pulse laser for nanolithography is an emerging technique which has been developed during the last three decades. The first steps came up in the 1990s, in which using a UV photosensitive polymer, is irradiated using a femtosecond laser beam in the NIR, in a phenomenon called two-photon-absorption [Maruo et al. 1997]. This polymer absorbs two photons at once, providing the same energy to valence electrons as a UV photon would do, creating radicals that propagate in the focal volume to produce an altered structure which is later developed.

Passing the years, other materials were used such as glasses and crystals, with good mechanical properties, and high laser damage thresholds, where applicating very intense and focalised pulses with a femtosecond duration penetrate inside the bulk, where a photo-chemical modification in its structure is stablished, this process being equivalent to that of a photoresist in standard lithography. The wet etching of optical crystals as YAG in its surface was initially studied in the 60s [Basterfield 1969], however, until now the chemical effects of localized femtosecond pulse photo-modification of the optical crystal bonds, has not been studied in detail. In this case, laser modified volumes have a much larger wet acid etching rate, and a new type of 3D laser lithography is possible. The technique for producing nanofluidic channels inside crystals such as sapphire and YAG was recently demonstrated by Ródenas et al. [Ródenas et al. 2019].

2.3 Simulation methods

2.3.1 The two-modes model

There are different methods for treating an electromagnetic wave interacting with a pattern that can produce diffraction. Clausnitzer et al. introduced in 2005 a phenomenological method that predicts with very good precision the behaviour of binary gratings. In her own words:

"This paper describes in a very easy and intelligible way, how the diffraction efficiencies of binary dielectric transmission gratings depend on the geometrical groove parameters and how a high efficiency can be obtained. The phenomenological explanation is based on the modal method. The mechanism of excitation of modes by the incident wave, their propagation constants and how they couple into the diffraction orders helps to understand the diffraction process of such gratings and enables a grating design without complicated numerical calculations".

In essence, the model is very similar to simply the propagation of modes interacting by their evanescent field as, for example, in a Match-Zehnder interferometer waveguide structure. See Fig. 2-4a, from [Clausnitzer et al. 2005] to have an idea about the light propagation.

2.3.2 The RCWA algorithm. RSoft: DiffractMOD software

The Rigorous Coupled Wave Analysis, RCWA, was proposed by M. Moharam and T. Gaylord [Moharam and Gaylord 1981] in the 80s as an alternative way to solve Maxwell's equations using eigenvalues instead of numerically, used in light interaction with structures, as diffraction gratings. This technique has been continuously improved till today, now being a mature algorithm [Bonod and Neauport 2016]. The model starts from Maxwell's equations in the differential way, includes boundary conditions and periodicity structure, and introduces a transmission-line treatment and the Bloch's theorem. In addition to this, Maxwell's equations can be understood as a lineal system $\mathbf{Ax} = \xi\mathbf{x}$, where $\mathbf{A}$ are their derivatives; $\mathbf{x}$ is a vector, in this case the magnetic and electric fields; and ξ the eigenvalue. Also, these solutions are calculated in the Fourier domain and the grating geometry is not treated as a whole, but only some regions are computed, taking advantage from the periodical nature of the structures [Synopsys 2020].

The simulations of this Master's Thesis were carried out by the software DiffractMOD, an extension of the commercial RSoft platform. Two-dimensional (2D) models can be done (also 3D ones) by a CAD environment and, simulating electromagnetic waves under a $\vec{k}$ vector and configurating other parameters, like the system spatial resolution and the light angle. In particular for this last one, a wavenumber vector of an incident planewave, in the most general case, can fall upon a surface according to the angle convention shown in Fig. 2-4b. In 2D simulations, only θ angle can be modified, while $\varphi = 0°$ and is deactivated.

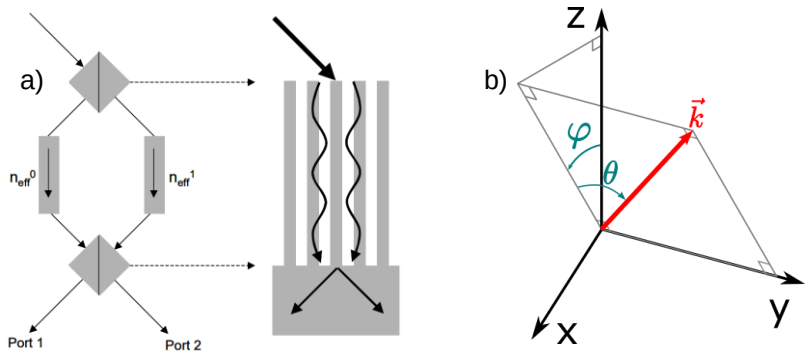

Figure 2-4. **a)** A diffraction grating in which two modes pass through it can be extrapolated to a Mach-Zehnder interferometer [Clausnitzer et al. 2005]. **b)** RSoft angle convention.

The seminal results obtained by Ródenas et al. on subwavelength diffraction gratings [Ródenas et al. 2019] were simulated (the theoretical part) by using the Two-Mode model described before, and a Finite Element Model (FEM). In this Master's Thesis work, the RCWA model (using DiffractMod) is used for the analysis of gratings, being compared the given results with those of the original paper. This first test allows us to validate the calculations.

2.4 Grating design methodology

This thesis work focuses on the new kind of transmission diffraction gratings in volume made in crystalline materials by means of fs-pulse 3D laser writing. Especially, the grating is made of two fundamental materials, YAG (yttrium aluminium garnet, $Y_3Al_5O_{12}$), a crystal with an orthorhombic slightly distorted symmetry (whose refractive index is $n_{YAG}(\lambda)$ [Hrabovský 2021]); and air (n_{air} considered constant), both dielectric materials. As the gratings consist of air nanopores inside YAG crystal, both the grating cover and substrate are made of YAG. Nanopores are done by means of drawing straight lines inside the crystal and can have various widths and heights, depending on the laser scan parameters and also the etching times considered. All the work performed here takes into account realistic grating parameters, mimicking the real width, heights, and also rounded shapes, of fabricated gratings. This is the first time that such a studyis ever performed, at least as far as is known. A sketch of this kind of diffraction gratings is showed in Fig. 2-5 (right).

Work strategy: Results on the simulation, fabrication and characterization of subwavelength gratings given by [Ródenas et al. 2019] and [Alessi et al. 2019] were checked and used. With the aim of familiarizing with the software and start with a solid basis of gratings previously studied by other methods,

simulating a diffraction grating with a 700 nm of pitch, a height of 1940 nm, 165 nm, illuminated by a plane wave of 1070 nm, TE polarization, and in Littrow configuration was made at first. Once this was mastered, and results were equal to those previously obtained by Ródenas et al., the work changed for studying the effects of introducing more realistic pore shapes in the calculations (with circular corners instead of perfectly square). For this reason, circular pore shapes were added at the ends of the flat-edged cylinders, to mimic a real laser written pore, having a shape comparison between them in Fig. 2-5a-c (right). It was seen that diffraction efficiency spectra resulted slightly better with circular borders. This round-edged design (Fig. 2-5b, right) is correct up to 250 nm, within the thesis work. For shallower pores, flat-edged pores had to be used (Fig. 2-5a, left), because the CAD modelling implementation, which was used did not work for those larger size ratios, producing distorted unrealistic shapes whose results needed to be discarded.

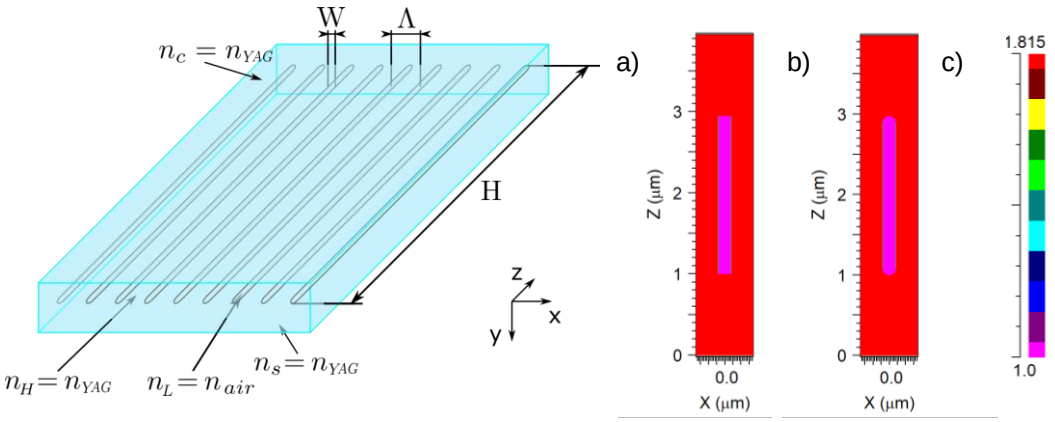

Figure 2-5. Left: sketch of a transmission diffraction grating volume indicating its parameters and refractive indices according to the notation on. Right: Cross sections of refractive index colourmaps for two different pore designs. **a)** flat-edged pore; **b)** rounded edges; **c)** Refraction index colour legend.

A height-to-width optimization for 700 nm, 500 nm and 300 nm pitches was made, according to different Littrow mountings (to obtain the best diffraction efficiency for target wavelengths), with the purpose of getting the shallowest grating pores which imply faster fabrication times, but also to study the utility of this kind of gratings for having a very high diffraction efficiency at different light wavelength ranges, from the NIR to the VIS and UV, thanks to the good transparency of YAG. Furthermore, an angle study was made to check the grating efficiency robustness against angle variations. Finally, some parameters that are usual in diffraction gratings characterization are studied. All these results are presented within the next chapter.

2.5 References

[Alessi et al. 2019] Alessi D.A., Nguyen H.T., Britten J.A., Rosso P.A. and Haefner C., (2019). Low-disperssion low-loss dielectric gratings for efficient ultrafast laser pulse compression at high average powers. *Optics and Laser Technology*, **117**, pp. 239-243.

[Basterfeld 1969] Basterfeld, J., (1969). The chemical polishing of yttrium iron garnet. *J. Phys.*, ***2***, pp. 1159–1161.

[Bonod and Neauport 2016] Bonod N. and Neauport J. (2016). Diffraction gratings: from principles to applications in highly-intensity lasers. *Advances in Optics and Photonics*, **8**(1), pp. 1-44.

[Born and Wolf 1980] Born M. and Wolf E., (1980). *Principles of Optics.* Pergamon Press.

[Cui 2005] Cui Z., (2005). *Micro-Nanofabrication: Technologies and Applications*, Higher Education Press, Springer.

[Clausnitzer et al. 2005] Clausnitzer T., Kley E.-B. and Tünnermann A., (2005). An intelligible explanation of highly-efficient diffraction in deep dielectric rectangular transmission gratings. *Optics Express*, **13**(26), pp. 10448-10456

[Clausnitzer et al. 2008] Clausnitzer T., Kämpfe T., Kley E.-B., Tünnermann A., Tishchenko A.V. and Parriaux O., (2008). High-dispersive dielectric transmission gratings with 100% diffraction efficiency. *Optics Express*, **16**(8) pp. 5577-5584.

[Erdogan 2021] Erdogan T., (2021). *PGL Technical Note–The Grating Equation.* Plymouth Grating Laboratory.

[Halir et al. 2014] Halir R., B.J. Przemek, Cheben P., Ortega-Moñux A., Alonso-Ramos C., Smith J.H., Lapointe J., Xu D., Wangüemert-Pérez J.G., Molina-Fernández I. and Janz S. (2014). Waveguide sub-wavelength structures: a review of principles and applications. *Laser & Photonics Reviews*, **9**(1), pp. 25-49.

[Hrabovský 2021] Hrabovský J., Kučera M., Paloušová L., Bi L., Veis M., (2021). Optical characterization of $Y_3Al_5O_{12}$ and $Lu_3Al_5O_{12}$ single crystals, *Opt. Mater. Express*, **11**, pp. 1218-1223.

[Magnusson 2007] Y. Ding and R. Magnusson, (2007). Band gaps and leaky-wave effects in resonant photonic-crystal waveguides, *Optics Express*, **15**, pp. 680-694.

[Maruo et al. 1997] Maruo S., Nakamura O. and Kawata S., (1997). Three-dimensional microfabrication with two-photon-absorbed photopolymerization, *Optics Letters*, **22**(2), pp. 132-134.

[Moharam and Gaylord 1981] Moharam M. and Gaylord T., (1981). Rigorous coupled-wave analysis of planar-grating diffraction. *J. Opt. Soc. Am.* **71**, pp. 811–818.

[Palmer 2020] Palmer C., (2020). *Diffraction grating handbook.* MKS Instruments, Inc., Richardson Gratings.

[Ródenas et al. 2019] Ródenas A., Gu M., Corrielli G, Paiè P., Sajeev J., Kar A.K. and Osellame R., (2019). Three-dimensional femtosecond laser nanolithography of crystals. *Nature Photonics*, **13**, pp. 105–109.

[Rumpf 2020] Rumpf R., (2020). *Subwavelength gratings.* [PowerPoint presentation]. University of Texas at El Paso (UTEP).

[Shimadzu 2021] Shimadzu, (2021). *The Grating Equations.*

[Synopsys 2020] Synopsys, (2020). *RSoft Photonic Solutions. DiffractMOD RCWA, User Guide*.

[Wang et al. 2009] Sang T., Wang L., Ji S., Ji Y., Chen H. and Wang Z., (2009). Systematic study of the mirror effect in a Poly-Si subwavelength periodic membrane. *Journal of the Optical Society of America A*, **26**(3), pp. 559-565.

CHAPTER 3. SIMULATION AND OPTIMIZATION OF SUBWAVELENGTH GRATINGS

3.1 First steps: checking previous results and improving the simulation

As mentioned in Chapter 2, the first goal of this Master's Thesis was to learn and develop a simulation method for laser-written subwavelength gratings based on the seminal results by Ródenas et al. [Ródenas et al. 2019], using RCWA algorithm in DiffractMOD software. The first goal is there to reproduce the optimal grating parameters for air nanopores that can diffract light with the maximum efficiency at the -1st order in transmission of 100% (theoretically) and that was reported by Ródenas et al., results which are presented in Fig. 3-1b.

In the previous work by Ródenas et al., a simulation was performed for the wavelength of 1070 nm (to match the experimental setup used therein), and this wavelength could not be changed due to the consuming time of performing each calculation at each wavelength for each grating's parameters. In this sense, the previous method used by Ródenas et al. was extremely time consuming, and there not very practical. The goal in this Master's Thesis is to develop a new workflow with which fast simulate gratings, quickly varying both gratings parameters as well as the test wavelengths, therefore allowing to truly develop gratings with all the required knowledge around them.

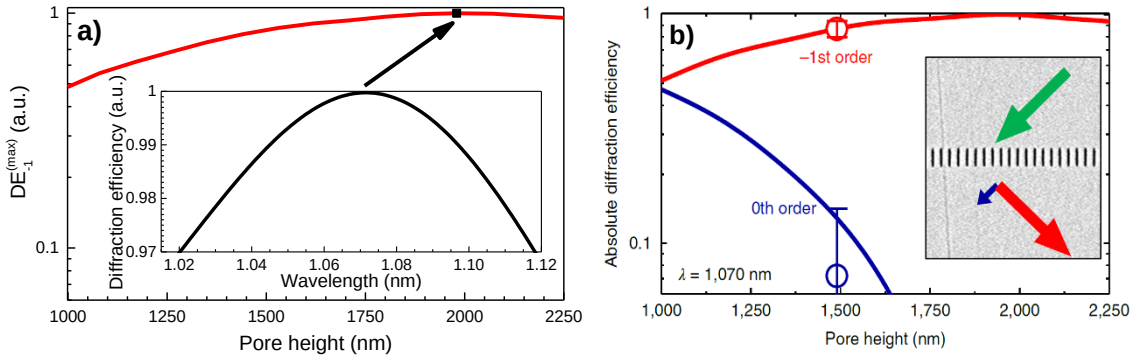

Figure 3-1. Diffraction efficiency curves depending on the pore height, fixed the pore width at 165 nm, in a diffraction grating of $\Lambda = 700$ nm, illuminated at 1070 nm under a Littrow configuration, $\theta_{Litt} = 24.9°$. **a)** Simulation of this work, for the -1st order, remarked the most efficient configuration. **b)** Simulations for 0th and -1st orders, including real results (in big dots). From [Ródenas et al. 2019].

Methodology validation: The first step was to replicate the original results. The simulation consisted in a diffraction grating made by air pores surrounded by YAG, with a 700 nm pitch, and whose width was of 165 nm as measured from SEM images (see inset in Fig. 3-1b). Ródenas et al. reported that for those grating conditions, the maximal absolute efficiency would be obtained for a large grating height of 1.98 µm, while experimental data obtained for around 1498 nm height was giving an efficiency of around 86% (-1st order), and almost 0 for the 0th order. The simulation done by our method, gave virtually the same results (see Fig. 3-1a) after many trials and errors on the method. This first positive result was key to prove the validity of all results.

High-efficiency bandwidth studies: Very importantly, we could also check the efficiency of the grating with respect to incoming light wavelength, something which had never been done before (see inset in Fig. 3-1a). Considering the efficiency of the grating to be above 97% (extremely high efficiency, at the state-of-the-art), we obtained a spectral bandwidth of $\Delta\lambda \sim 100$ nm, this implying that this type of gratings has a great potential for high-power ultra-short femtosecond pulse technology, where the laser pulses are very broadband. To give a general example, following the equation $\Delta\tau = \frac{TBP}{c}\frac{\lambda^2}{\Delta\lambda}$, where TBP is the Time Bandwidth Product parameter which depends on the shape of pulse, a laser pulse at a wavelength of 1 μm that has a spectral width (Gauss shape, $TBP = 0.441$) of 100 nm, will then have a pulse duration of 14.7 fs, i.e. extremely short femtosecond pulses (this is discussed in the Appendix). Equally, if for example the gratings were to be used in an ultrashort pulse Ti:Sa mode-locked laser system, the wavelength would be around 808 nm, and for a pulse bandwidth of 100 nm, the pulse duration would then be of just 9.6 fs. If gratings with efficiency above 97% could be used, overall losses would be low, and a high pulse energy system could be developed.

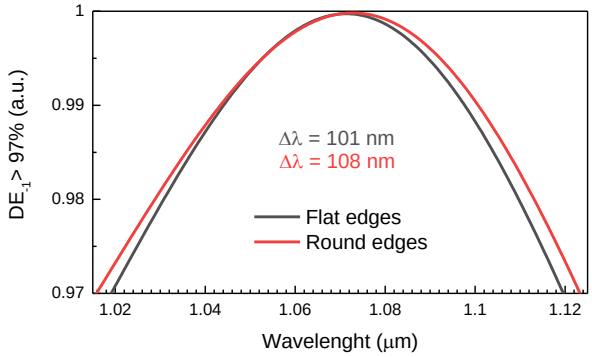

Figure 3-2. Diffraction efficiency spectra over 97% for a diffraction grating illuminated at $\theta_{Litt} = 24.9°$ with a pitch $\Lambda = 700$ nm and optimized at 1070 nm, rounded vs squared nanopore edges.

Pore shape effects: The effect of the pore shape was also investigated (squared corners or rounded corners) in order to discover which shape optimizes any given aspects of the grating behaviour (bandwidth, efficiency…). The pore shape chosen for this simulation, was almost equal to the real fabricated ones (see Chapter 2, section 2.4, Fig. 2-4 right), whose borders are rounded and not squared like in a simplified grating structure, imitating the laser writing effect which produces rounded effects. It was found that this enhances the diffraction efficiency and bandwidth respect a flat-edged pore, which is a very positive finding. A numerical comparison is plotted in Fig. 3-2, where for a fixed width pore of 200 nm (this being the standard nanopore shape that can be achieved in reality in the laboratory), the optimal height was identified (according to that giving maximum efficiency for a given wavelength), slightly different in flat-edged and rounded-edged approximations (1.629 μm and 1.675 μm respectively), and an improvement of 7% was found for rounded vs squared nanopore cross-sections.

3.2 Width and height pore optimization

The next step was to do a study to obtain the best pore configurations, whose maximum efficiencies are reached at different approximate wavelengths of interest (1070 nm, 800 nm and 500 nm), presented in Fig. 3-3.

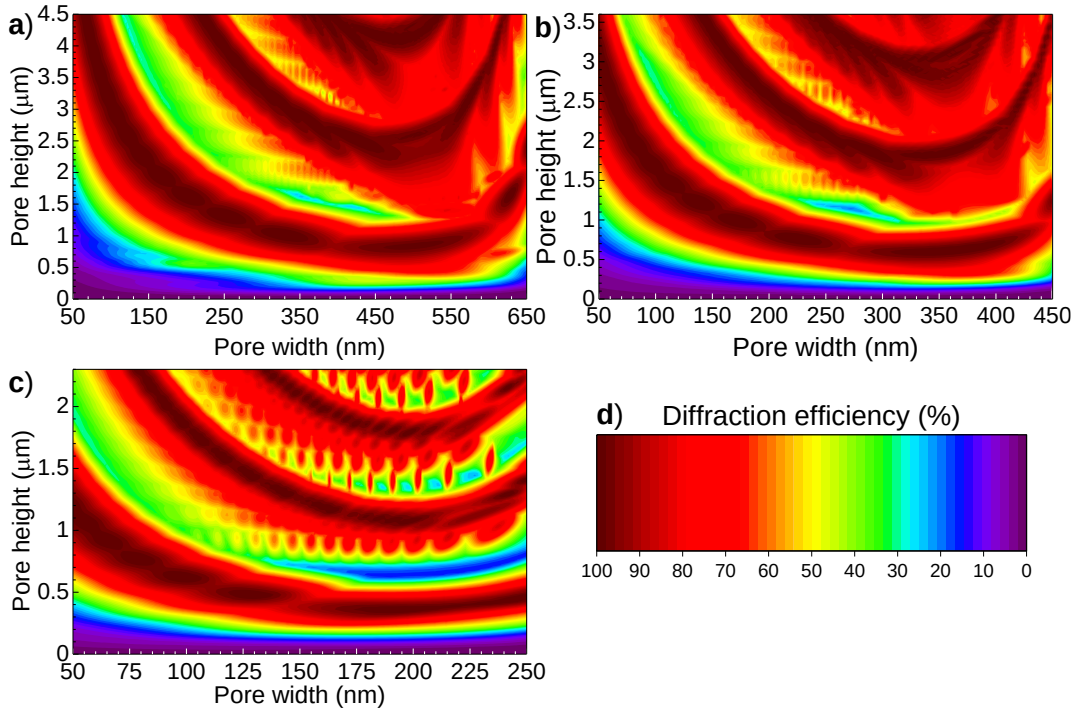

Figure 3-3. Colourmaps of optimized pore sizes (plotting its height as a function of its width), in which its diffraction efficiency (at -1st order in transmission) is maximum, at different conditions: **a)** $\lambda_0 = 1070$ nm, $\theta_{Litt} = 24.9°$, $\Lambda = 700$ nm; **b)** $\lambda_0 = 800$ nm, $\theta_{Litt} = 26.1°$, $\Lambda = 500$ nm; **c)** $\lambda_0 = 500$ nm, $\theta_{Litt} = 26.9°$, $\Lambda = 300$ nm; **d)** colour scale.

The first simulation (Fig. 3-3a) was made optimized for 1070 nm light, fixing the previous grating period at 700 nm and, doing a scan for several pore sizes, starting from 0.1 µm height (this lower limit was chosen to check the simulation) to a 4.5 µm of height, with a path of 30 nm; while a width varying from 50 nm to 650 nm, with a step of 3 nm, for which the maximum efficiency was recorded for each parameter map vector. For the second one (Fig. 3-3b), for 800 nm wavelength light, the pitch is smaller, $\Lambda = 500$ nm, so the pore width will be smaller than in the previous simulation, from 50 nm to 450 nm, with a step of 3 nm, while for the pore height goes from 0 µm to 3.5 µm with a 30 nm step. Finally, for the third case optimized for visible 500 nm wavelength light (Fig. 3-3c), with a $\Lambda = 300$ nm, pore width is chosen from 50 nm to 250 nm, step at 1 nm and, the pore height changes each 2 µm, from 0 µm to 2.3µm.

Seeing at Fig. 3-3a, well defined regions where the diffraction efficiency is much higher than others are clearly identified, those would be the target fabrication parameters. Especially, for 3DLW purposes, all ranges available in the simulation cannot be reproduced. Pore widths around $100 - 200$ nm are preferred as they can be written on a single scan, which means shorter fabrication times. Pore sizes for the best diffraction efficiency can be well-reproduced for laser writing, having some satellite-shaped island regions where in a tight range variations of pore dimension can enhance the $DE_{-1}^{(\max)}$ up to 100% at 1070 nm wavelength centred. As an example, if a pore width of 167 nm is selected, an optimal pore of 1.98 µm is observed, in consonance with the simulation in the previous section, using the same illumination conditions and pitch. In addition to this, another very promising pore size for laser writing is obtained at 200 nm width, 1.675 µm height, whose diffraction spectrum is seen in Fig. 3-2 (red line). In this case, the bandwidth is 108 nm. This case was previously presented as an example. This efficiency maps are therefore

very informative and, depending on the nanopore shapes and cross-sections (heights and widths), an optimal grating period can be chosen. The larger the period also the better regarding fabrication quality: shorter fabrication times are always better, but also the shorter the fabrication times the more precise the grating will be.

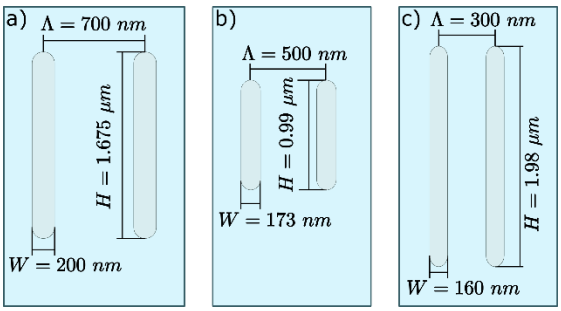

Figure 3-4. Sketches of optimized pores for $DE_{-1}^{(\max)} > 0.9999$ at different configurations. **a)** $\theta_{Litt} = 24.9°$, $\Lambda = 700$ nm; **b)** $\theta_{Litt} = 26.1°$, $\Lambda = 500$ nm; **c)** $\theta_{Litt} = 26.9°$, $\Lambda = 300$ nm.

In Figs. 3-3b and c, other Littrow mounts and pitches were chosen for different wavelengths of 800 nm and 500 nm, specifically, at $\theta_{Litt} = 26.1°$, $\Lambda = 500$ nm and $\theta_{Litt} = 26.9°$, $\Lambda = 300$ nm, respectively. For both of them were found out that maximum theoretical DE_{-1}, centred at $\lambda_0 = 800$ nm in b) and $\lambda_0 = 500$ nm in c), is over 99.9% in some regions, as in the first case (Fig. 3-3a). Some interesting configurations are, for b), a pore size with a 173 nm width and 0.99 µm height. For c), even though there are regions with better efficiencies, there is only one with proper dimensions for writing, which is at width 160 nm and height 1.98 µm. These characteristic maps do also coincide with general grating behaviours found in the literature [Clausnitzer et al. 2008].

Bandwidth investigation: Finally, it was studied for diffraction efficiency spectra, the bandwidth at $DE_{-1} > 97\%$, for gratings periods of 700 nm and 500 nm, at $\theta_{Litt} = 24.9°$, $DE_{-1}^{(\max)}$ centred in 1070 nm and $\theta_{Litt} = 26.1°$, $DE_{-1}^{(\max)}$ centred in 800 nm respectively, with its pore width, resulting that $\Delta\lambda$ can suffer important changes among different pitches and, obtaining the largest values for the most spaced pores, a it can be seen in Fig. 3-5.

3.3 Angle study

In this last part, a comparison was made between the diffraction gratings of this work the state-of-the-art high efficiency surface relief diffraction gratings (in reflection) for ultra-short-pulse lasers, published very recently by [Alessi et al. 2019], studying its diffraction efficiency at -1st order and bandwidth, at incident angles with a difference of 4° among them, seeing in Fig. 3-6. The grating specifications of the paper consists in a pitch Λ of 1480 lines/mm (or 676 nm), a filling factor FF of 0.22 for the grating pillar, with a $\theta_{Litt} = 36.8°$. Input angles θ, φ combinations can be seen in Fig. 3-6b. For gratings presented in this thesis, Λ is 500 nm, or 2000 lines/mm, a FF of 0.34 and $\theta_{Litt} = 26.4°$, ($\varphi = 0°$ and fixed, due to software restrictions).

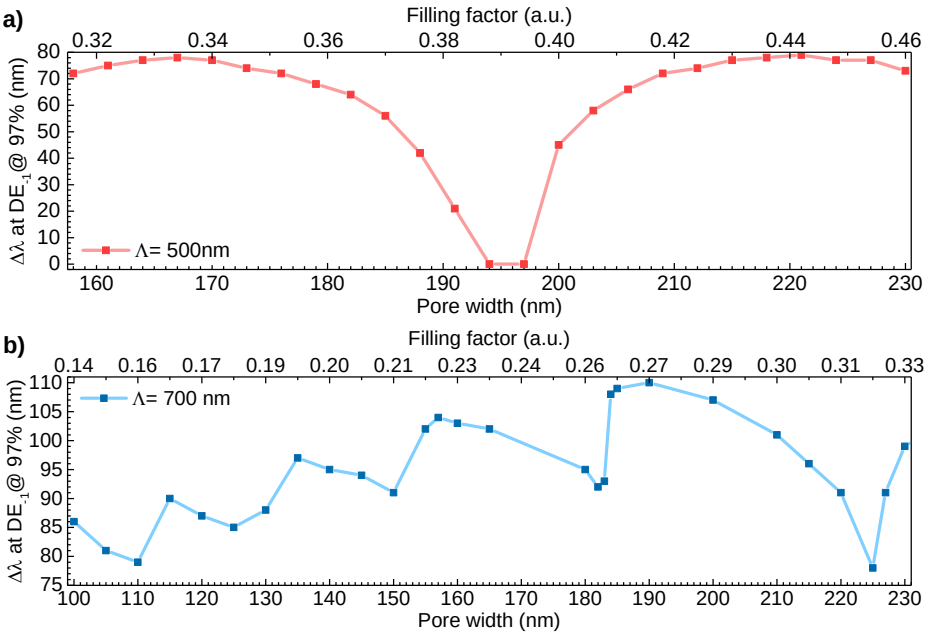

Figure 3-5. Bandwidths as a function of the width pore and filling factor, when the diffraction efficiency is above 97% for: **a)** $\lambda_0 = 800$ nm, $\Lambda = 500$ nm and $\theta_{Litt} = 26.1°$; **b)** $\lambda_0 = 1070$ nm, $\Lambda = 700$ nm, $\theta_{Litt} = 24.9°$.

Data of Fig. 3-6 is summarized in Table 3-1. At first glance, gratings made in this work present larger bandwidths than those made from Alessi et al. (around 400 nm in this work, against 120 nm Alessi et al.), around three times larger at Littrow angle, while maxima diffraction efficiencies are qualitatively the same. Besides, when θ is increased four degrees, this work gratings maintain a wide bandwidth, even larger, but also $DE_{-1}^{(\max)}$ is higher than 96%, while for the others, fall around an 8%, up to 88%. And, although there is not any comparative for $\theta_{Litt} - 4°$, this work gratings also presents a wide bandwidth and great efficiency.

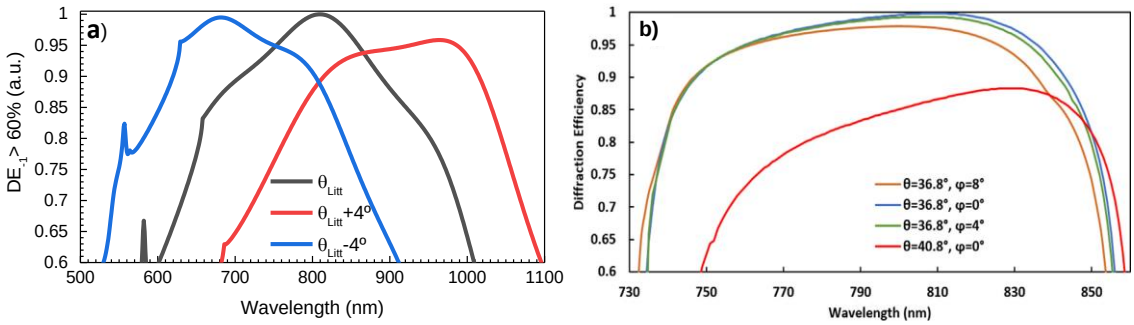

Figure 3-6. Angle comparison for a grating of $\Lambda = 500\ nm$, whose $DE_{-1}^{(\max)}$ is centred at 810 nm. **a)** results of this work, only varying the component $\theta \pm 4°$, centred at $\theta_{Litt} = 26.4°$ (FF=0.34); **b)** Changing different configurations of θ and $\varphi \pm 4°$, centred at $\theta_{Litt} = 36.8°$, (FF=0.22); (plot taken from [Alessi et al. 2019]).

Finally, a similar study was made for two pore configurations, with a grating period of 700 nm (using the design of this thesis), results given in Fig. 3-7. It was found out that when θ_{Litt} is four degrees smaller, the maximum diffraction efficiency decreases (as happens increasing this angle), but also the bandwidth increases almost 10 nm in both configurations.

Table 3-1. Comparison results extracted from Fig. 3-6.

Configuration and parameters	This work	[Alessi et al. 2019]
$\boldsymbol{\theta_{Litt}, \varphi = 0°}$	$\mathbf{26.4°}$	$\mathbf{36.8°}$
$DE_{-1}^{(\max)}$, λ_c	$> 99.5\%, 810$ nm	
$\Delta\lambda$ @ $DE_{-1} = 60\%$	408 nm	~120 nm
$\boldsymbol{\theta_{Litt} + 4°, \varphi = 0°}$	$\mathbf{30.4°}$	$\mathbf{40.8°}$
$DE_{-1}^{(\max)}$, λ_c	96%, 964 nm	88%, 830 nm
$\Delta\lambda$ @ $DE_{-1} = 60\%$	413 nm	~110 nm
$\boldsymbol{\theta_{Litt} - 4°, \varphi = 0°}$	$\mathbf{22.4°}$	--
$DE_{-1}^{(\max)}$, λ_c	99.5%, 862 nm	--
$\Delta\lambda$ @ $DE_{-1} = 60\%$	381 nm	--

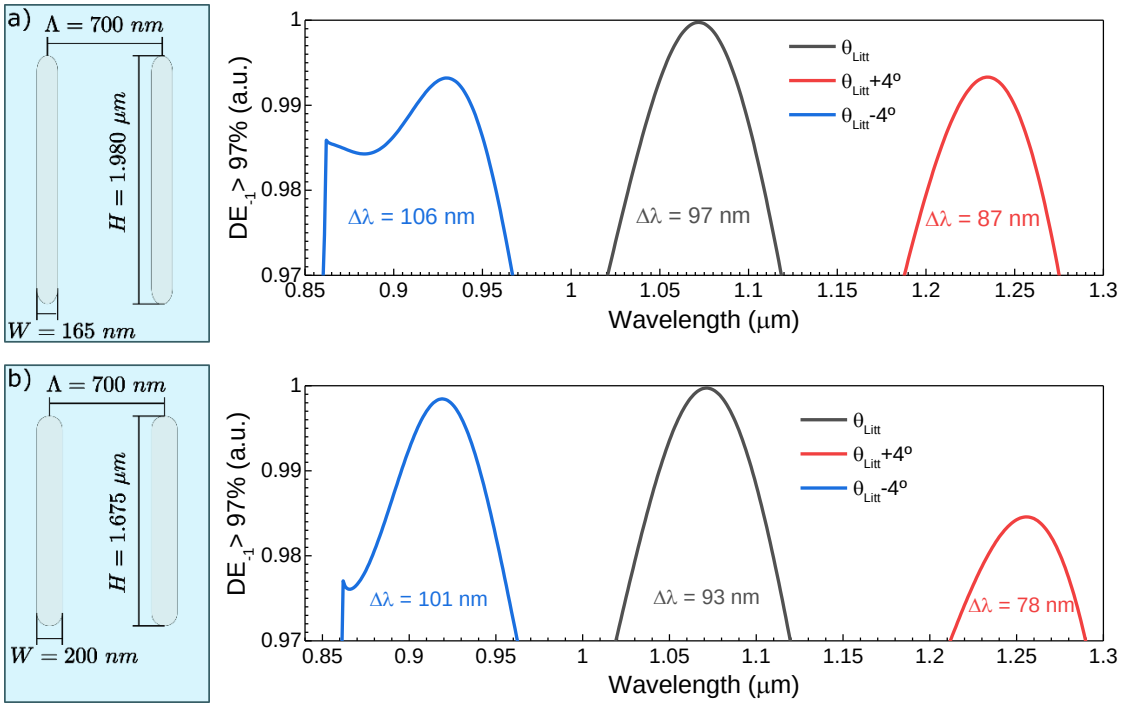

Figure 3-7. Comparison of diffraction efficiencies over 97% for two different grating configurations, fixing $\Lambda = 700$ nm, with optimal $\lambda_0 = 1070$ nm, varying the $\theta_{Litt} = 24.9 \pm 4°$. **a)** a pore of 1.98 µm of height and pore width of 165 nm; **b)** a pore height of 1.68 µm and pore width of 200 nm.

3.4 References

[Alessi et al. 2019] Alessi D.A., Nguyen H.T., Britten J.A., Rosso P.A. and Haefner C., (2019). Low-disperssion low-loss dielectric gratings for efficient ultrafast laser pulse compression at high average powers. *Optics and Laser Technology*, **117**, pp. 239-243.

[Clausnitzer et al. 2008] Clausnitzer T., Kämpfe T., Kley E.-B., Tünnermann A., Tishchenko A.V. and Parriaux O., (2008). High-dispersive dielectric transmission gratings with 100% diffraction efficiency. *Optics Express*, **16**(8) pp. 5577-5584.

[Ródenas et al. 2019] Ródenas A., Gu M., Corrielli G, Paiè P., Sajeev J., Kar A.K. and Osellame R., (2019). Three-dimensional femtosecond laser nanolithography of crystals. *Nature Photonics*, **13**, pp. 105–109.

CHAPTER 4. CONCLUSION

4.1 Summary

To sum up this thesis, an emphasis was made for subwavelength diffraction gratings, introducing them, presenting its fundamentals, and exposing some applications, in first chapters, but not before getting an overview of the different technologies available. A new fashion of volume subwavelength diffraction gratings, embedded in a crystalline material, and optimized for -1st order in transmission were analysed, using simulations to recreate the behaviour with certain light conditions, concluding that in fact, they overcome other novel gratings in literature, in diffraction efficiency and spectral ranges. What is more, in the following chapter, an in-process setup was presented for the intention to fabricate them and, stablishing a fabrication method which could be extrapolated in the industrial field. An optical characterization allowed to improve and understand the operation of some devices involved in this setup.

All this indicates that this kind of diffraction gratings are very appealing in the future for new and exciting usages, being able to look forward scientific installations and, in consequence, letting that science progresses with newly discovers.

4.2 Future work

Plenty of work remains to be done. The next critical step will be the competition of the setup assembly, including the correct working of all components that are not yet configured. The automatization for security elements that avoid fabrication problems, as well as a proper calibration. The pulse picker should be synchronised with the train pulse offered by the Ti:Sa laser; for this reason, a communication must be stablished between these drivers. The next step will be a study about the laser lithography writing in the material, adjusting the best times to obtain the desired patterns presented in Chapter 2. Post writing steps, as etching times and acid composition must be studied. So, the main aim will be to reproduce simulation designs, contrasting results given by RCWA method and experimental measurements. Besides, a threshold damage tests should be really interesting, comparing them with others that are being commercialized. Finally, these gratings could be made by other materials, for this reason, new simulations should be done, as well as improve the current, i.e., with the geometry.

APPENDIX. DEVELOPMENT OF AN EXPERIMENTAL FABRICATION SETUP

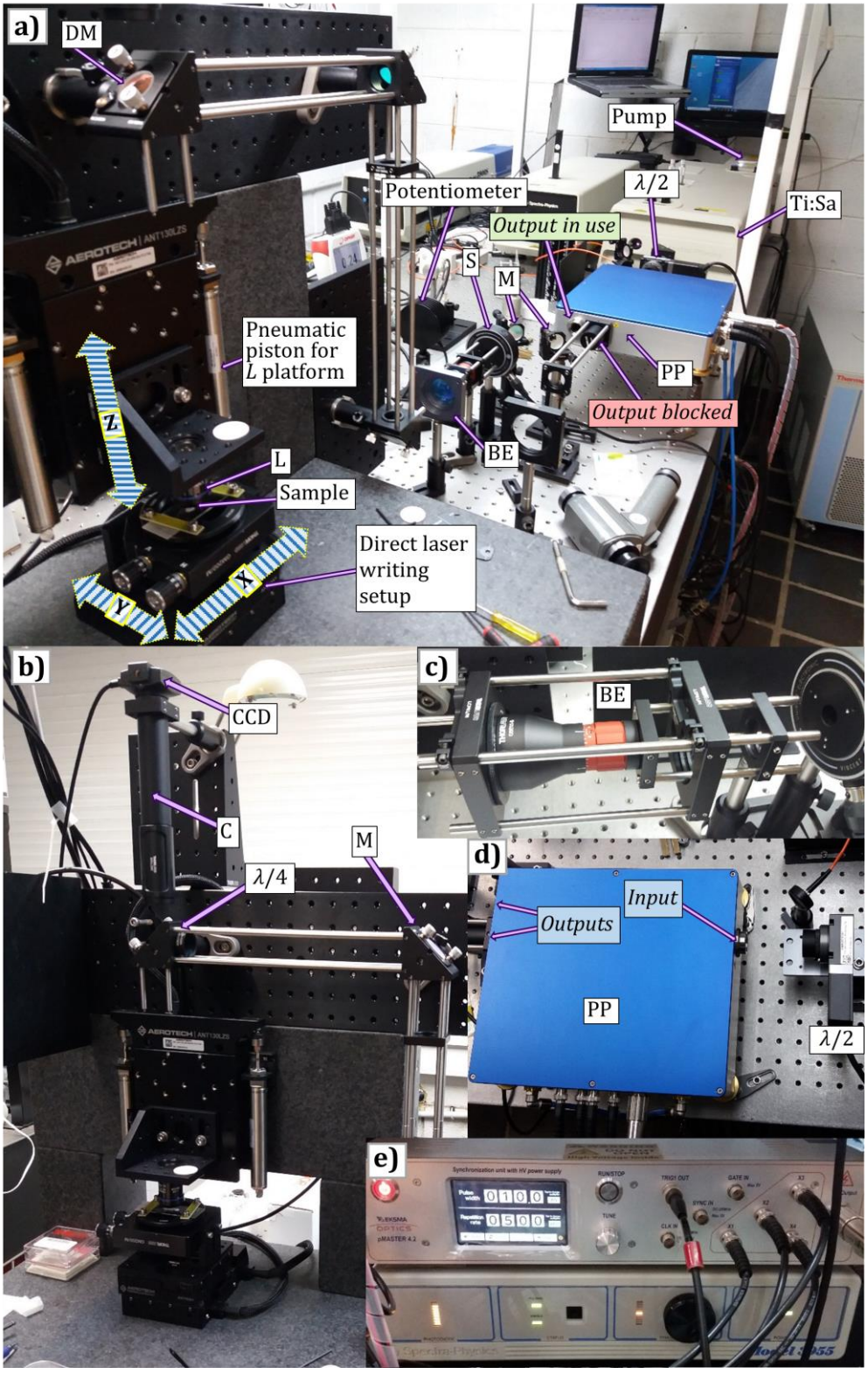

Figure A-1. **a)** 3D fs-laser nanolithography setup overview using the notation in List of Symbols and Abbreviations. **b)** Rest of the setup. **c)** Beam expander in more detail. **d)** Pulse picker overhead view. **e)** Pulse picker driver.

A.1 Femtosecond pulse fabrication setup

All the work introduced in the previous chapters is based on previous experimental results [Ródenas et al. 2019]. A new 3D laser writing (3DLW), also called 3D femtosecond-laser nanolithography has been developed at the laboratory during the 2021 year. During this thesis, the development of this new setup has been followed. This chapter reports on the introductory work which has been done to learn the basics of this setup and experimental technique. Figure A-1 shows a picture of the system working.

In Fig. A-2 the experimental setup developed is sketched, and which is composed of four functional sections: (1) fs-laser system; (2) pulse-picking and laser power control; (3) Nanopositioning, focusing and imaging system; (4) control and automatization. List of Symbols and Abbreviations is included in the beginning of thesis.

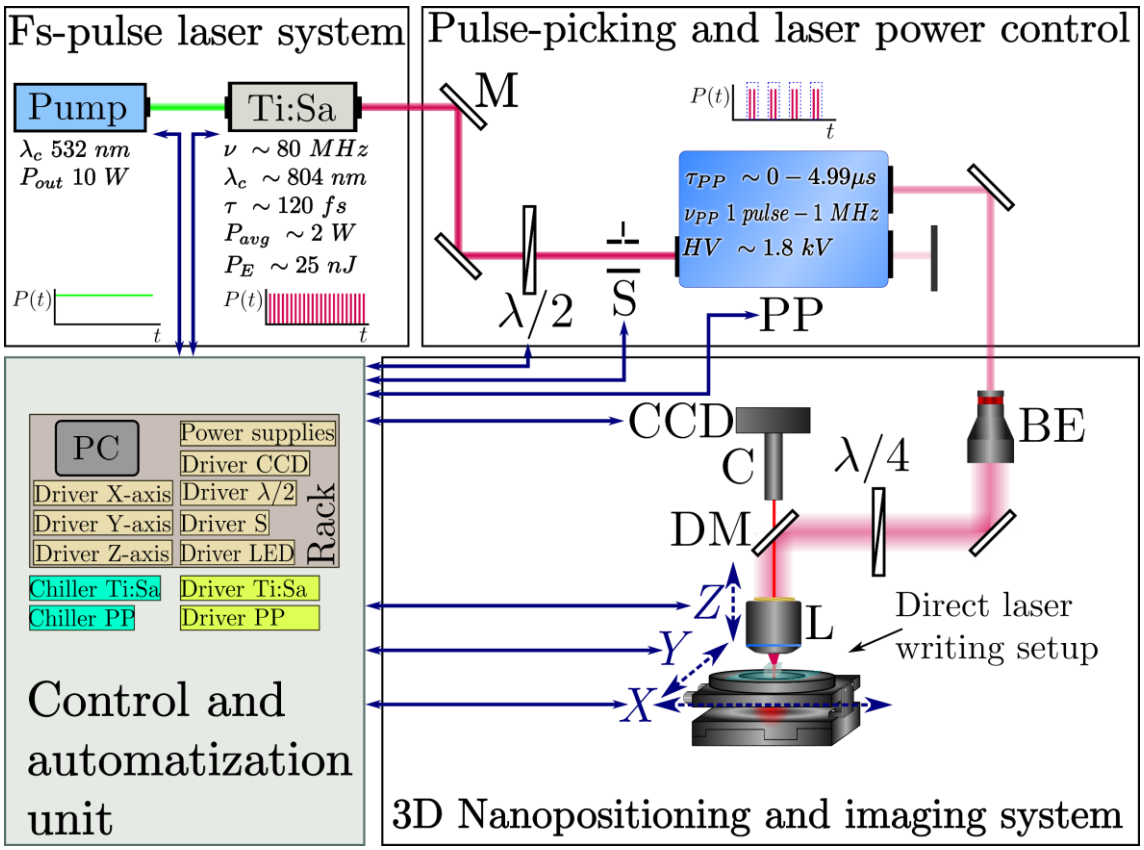

Figure A-2. Sketch of the setup for 3D-laser nanolithography, composed of 4 functional sections: (1) fs-laser system, (2) pulse-picking and laser power control, (3) 3D Nanopositioning, focusing and imaging system, (4) control and automatization.

A.1.1 Fs-pulse laser system

The setup is powered by a Millenia eV (Spectra-Physics) continuous wave laser emitting at 532 nm, delivering a maximum of 10 W output power, pumping a Ti:Sa Tsunami (Spectra-Physics) femtosecond-pulse laser in mode-locking configuration [Spectra 2002]. First, a power curve was measured, studying the input power powered by the pump laser, taking them from the software, and the output power,

given by the Ti:Sa Tsunami fs-laser, using a thermopile OPHIR 12A-v1 [Ophir 2021], placed not directly in the laser output, whose results are presented in Fig. A-3a. In this case, the pulse picker was switched off.

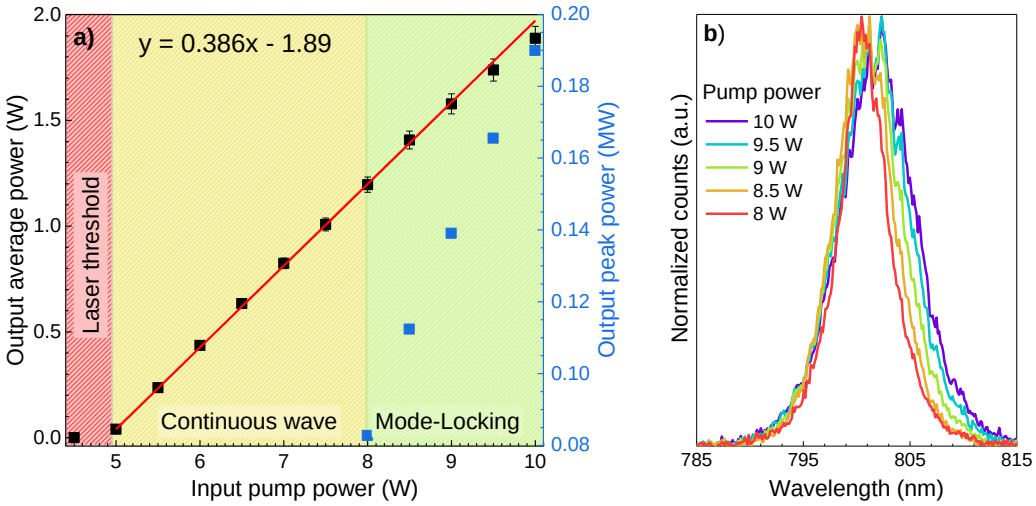

Figure A-3. **a)** Power curve of the laser pulse, plotting the average power (in black dots and *Y* axis) and the peak power (in blue dots and *Y* axis). **b)** Normalized spectra of Ti:Sa laser varying the pumping power.

The results are interesting, because three different regimes could be seen varying the pump power. The laser threshold was stablished in 5 W, lasing in continuous wave above this value, until reaching 8 W. In this regime, light is not emitted as a train pulse, as it happens after this power once the system starts to mode-lock. From 8 W to 10 W, laser enters in mode-locking, emitting pulses with a certain spectral width and temporal duration, which is slightly power dependent. As it can be seen in Fig. A-3a (blue axis), the peak power obtained is in the order of hundreds of kilowatts, having a linear dependence, whose fitting gives an average power ratio of $P_{out}^{(avg)}/P_{in} = 0.39$.

About the peak power calculations, they were calculated using the spectra in Fig. A-3b, whose data were fitted using the hyperbolic secant equation Eq. (A-1) [Uhlig 2015]:

$$\operatorname{sech}^2(\lambda) = \frac{I_0}{\cosh^2\left(\frac{\lambda - \lambda_c}{\Delta\lambda}\right)} \tag{A-1}$$

where I_0 is the maximum intensity; the barycentre, λ_c and $\Delta\lambda$ the spatial width of the pulse. The reason for not fitting to a gaussian pulse is in the Pearson coefficient (R^2), being slightly closer to the unit using Sech square fittings for the powers studied, shown in Fig. A-4. In Fig. A-3b is observed in spectra that decreasing the pumping power, bandwidths are lower. They were taken using an Ocean Optics spectrometer. In consequence, to estimate in first order of approximation the pulse duration Δt can be obtained by the Eq. (A-2).

$$\Delta t = \frac{\lambda^2}{c\Delta\lambda} \tag{A-2}$$

Having c as the speed of light. In addition to this, it must be applied a correction factor on τ given by the time-bandwidth product, $TBP = \Delta\lambda \cdot \tau$, whose value is ~ 0.315 if pulses have a sech^2 shape [Uhlig 2015].

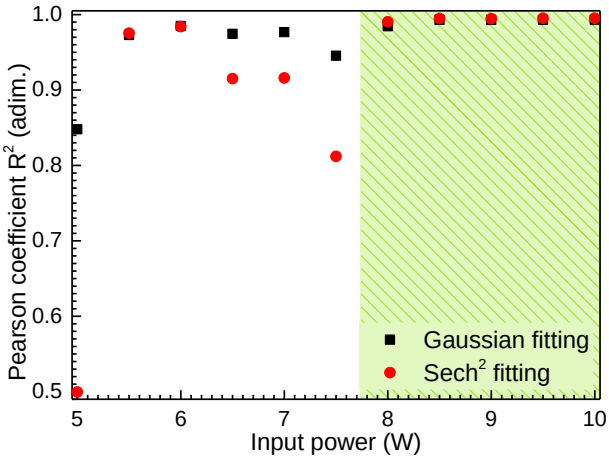

Figure A-4. Pearson coefficient for the fitting of the laser spectrum, as a function of the pump power (remarked in green the region of interest). Dots in black refer to data fitted using the gaussian expression, while in red dots are referred to sech^2 fitting.

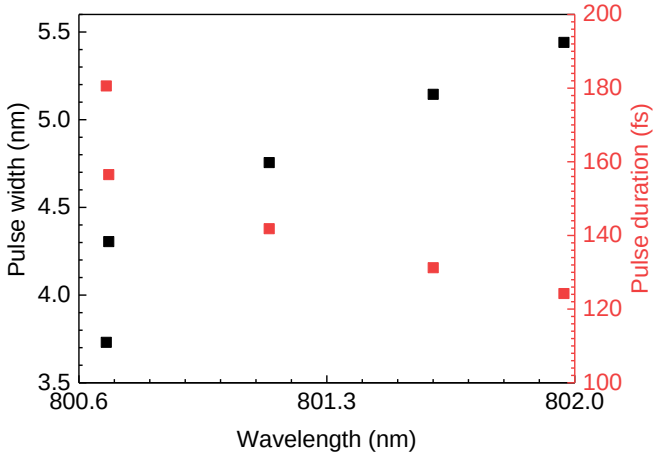

Figure A-5. Pulse spectral bandwidth (in black dots and *Y* axis) and estimated pulse duration (red dots and *Y* axis), using data fitting the results of the Fig. A-3b.

Then, the results presented in Fig. A-5. It happens that increasing the barycentre, the larger the bandwidth, the shorter the pulse duration, where the shortest at 124 fs. After that, the output peak power P_{peak} was calculated using the Eq. (A-3):

$$P_{peak} = \frac{P_{avg}}{\tau \cdot \nu} \tag{A-3}$$

with P_{avg} as the output average power (measured in the potentiometer), the pulse duration, or Δt, and ν the pulse repetition rate, 80 MHz using this device. In consequence, for 3DLW, which is necessary ultrashort and truly energetic pulses, the best pump power is the maximum, 10 W, because of offering the highest possible pulse energy, which is critical to produce modification in the material.

A.1.2 Pulse-picking and laser parameters control

Once is characterized the lasing system, a digital controlled half waveplate ($\lambda/2$ or HW) placed in a rotator which is controlled via software was characterized, controlling the light passed through it according to its angle orientation. This kind of optical element produces a phase difference between the H and V polarized components of an electromagnetic wave and acts as a linear polarization rotator for

incoming linearly polarized light. As the pulse-picker (PP) has fixed internal thin-film polarizers, at the outputs of the PP the optical power will vary as a functional of the HW angle; this is presented in the Fig. A-6. Changing the rotator angle, a change in the power is observed by the thermopile, repeating maxima and minima each 90°, at both 10 W and 8.5 W pump power.

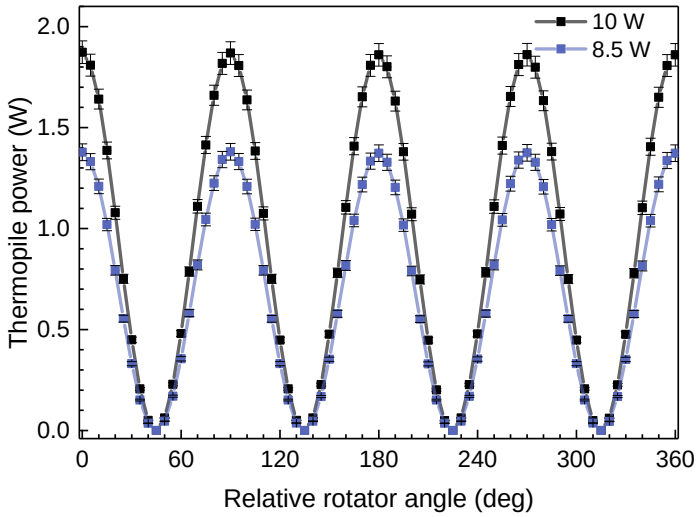

Figure A-6. Power curves varying the halfwave plate orientation. In black, pumping at 10 W, in blue, at 8.5 W.

The PP [Eksma 2020] is another important control element in the setup. This device allows to select, from the fundamental fs-pulse train given by the Ti:Sa laser, either individual pulses or a new pulse frequency of up to 1 MHz, by means of using a Pockels cell. The pocket cell is made of a nonlinear optical material, KTP crystal (Potassium Titanyl Phosphate), in which is applied a high voltage to create birefringence, which in turn rotates the incoming polarization. The phase difference is linear depends on the light wavelength, the refraction index of the material, and the voltage applied. The PP of the setup has two outputs. When there is not any voltage applied, the light goes out the port parallel to the input, and otherwise when it is switched on, due to internal polarizers. All values are controlled by its driver, where are settled the working parameters to create and repeat pulse windows. The most important are the time window or pulse duration (or pulse width) τ_{PP}, the number of pulses that will be inside the window, given by time units; the pulse repetition rate or frequency ν_{PP}, in frequency units; and the high voltage value, that must be configurated in 2.1 kV (current below 5 mA), cooled down at 22 °C with a small chiller unit.

In Fig. A-7 is presented an oscilloscope trace produced by the pulse picker, acquired by a Hamamatsu S5971 silicon diode, and a Rigol DS1202Z-E oscilloscope. Each window has a pulse width (τ_{PP}) of 125 ns, repeating each 100 kHz (ν_{PP}) (or 10 µs). In this configuration, inside each window must have ten pulses that supplies the Ti:Sa laser, because its ν is 80 MHz (or 12.5 ns time between pulses) [Spectra 2002]. In fact, in Fig. A-7b corroborates that. Another important factor that changes is the average power measured out the pulse picker, because the more pulses pass, the higher the average laser power, given by Eq. (A-4):

$$P_{PP}^{(avg)} = \frac{P^{(avg)} DC}{100} \tag{A-4}$$

where $P_{PP}^{(avg)}$ is the average power when windows are created, $P^{(avg)}$ is gotten when the pulse picker is switched off and DC is the Duty Cycle (dimensionless, expressed in percent), given by the ratio: $DC = 100 \cdot \tau_{PP}/\nu_{PP}$ (both of them measured by the thermopile) [Lyons 2017]. So, for the previous configuration, $DC = 100 \cdot 125\ \text{ns}/10\ \mu\text{s} \approx 1.3\%$, result in sense with the experimental value, around 39 mW when picking pulses, versus 1.8 W when was switched off.

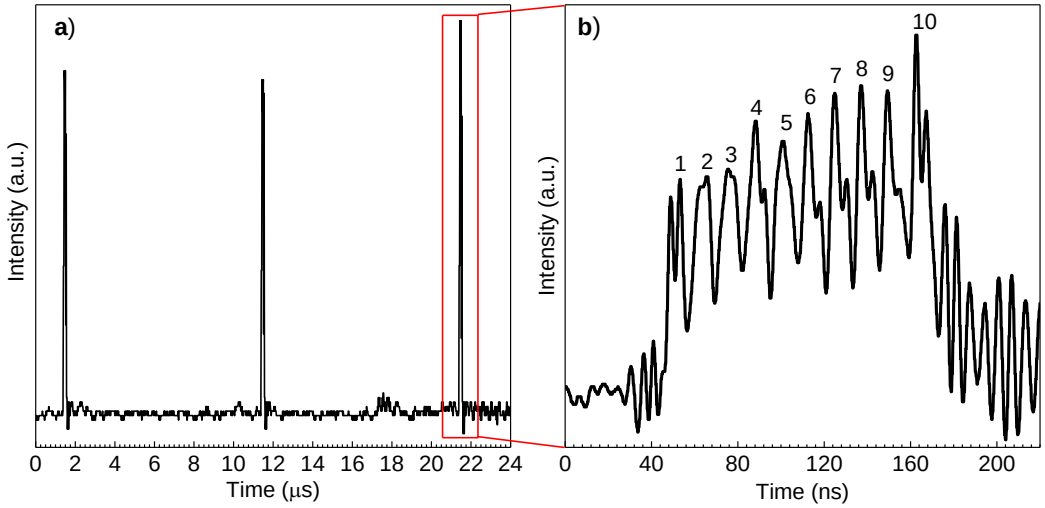

Figure A-7. Oscilloscope trace of a window with a τ_{PP} of 125 ns and a ν_{PP} of 100 kHz. **a)** Three windows; **b)** Zoom of a certain window, counting individual pulses.

A.1.3 3D Nanopositioning and imaging system. Direct laser writing setup

Once pulses are selected in the windows made by the pulse picker, they pass through a beam expander. This device is a kind of telescopic system that can increase the width of the laser beam by five times, from a beam width (measured at $1/e^2$ intensity) of < 2 mm to a beam of 10 mm. This part is crucial for exploiting the full numerical aperture (NA) of the focusing objective, as light must fill the totality of the microscope entry, to obtain the full NA. A quarter waveplate ($\lambda/4$ or QW) is also optically used before the objective, if circular polarization needs to be used for fabrication instead of linear polarization. The polarization state of fs-pulses will influence the type of non-linear ionization regimes (multi-photon absorption and avalanche ionization), and it has been observed that the shape of nanopores greatly depends on the polarization state. Furthermore, a circular polarization state allows to decouple the polarization direction and the scanning directions, something important if different 2D and 3D laser trajectories are going to be used [Ródenas et al. 2019].

The direct laser writing setup (Fig. A-8) is the part in which pieces will be placed for writing. An Aerotech A3200 software is used to either control manually or automatize (coding orders), using nanopositioning stages that cover three dimensions, and its respective drivers, whose models are given in Table A-1 [Aerotech 2018]. Their characteristics, a step resolution of 1 nm, with a maximum speed and acceleration of 10 mm/s and 25 cm/s^2 respectively; for X and Y axes can handle a weight of 0.5 kg while for Z axis up to 1 kg. The motors are powered from the drivers, but power supplies are external, also connected to the drivers, needing 48 VDC and 5 A_{rms}. Drivers, that control the movement, temperature,

electrical values, and communicate among other drivers, work at 24 VDC, 2 A. This issue was solved using independent power supplies that feed motors and drivers independently. The user can monitor the writing process through a camera system placed behind the last mirror which is backpolished and partly transmits visible light [Thorlabs(OC) 2021].

Table A-1. Labels for motors involved.

Hardware Axis Designation	Type of motor	Driver model
Axis-1 (X) Lower Axis-2 (Y) Upper Axis-3 (Z) Vertical	ANT95-25L BLMUC-95-A	XC2-10-EB1-MX1-PSO1

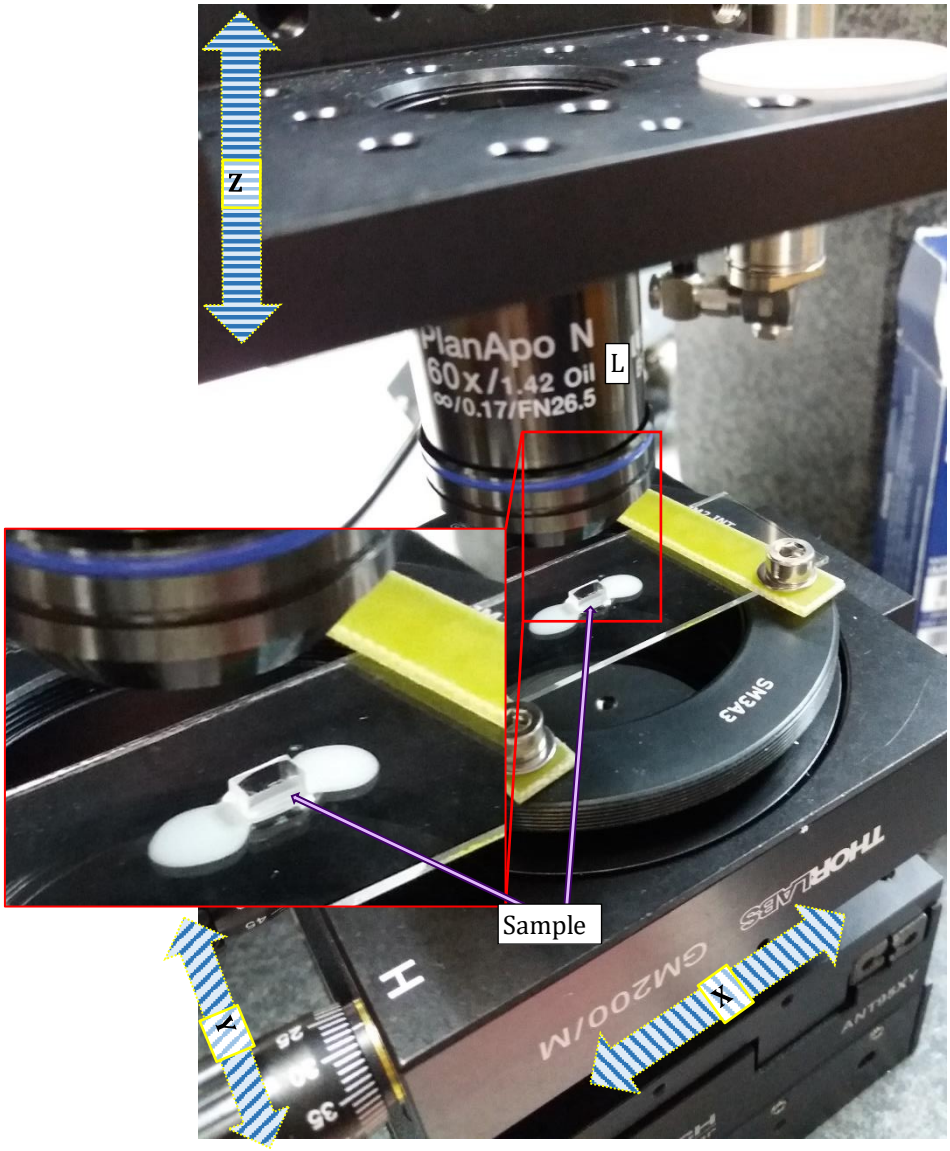

Figure A-8. Direct laser writing setup with sample zoomed.

A.1.4 Control and automatization part

In Fig. A-2 are several dark blue arrows that connect some devices to a rack. Inside this element has been placed the drivers, to organize and reduce the dust. Picture of this installation is placed in Fig. A-9. Drivers are in turn controlled by an industrial computer, by a software property of Aerotech, the A3200.

Also, code programs can be written in G-code, to implement programs and sending orders to these devices, with the purpose of automatizing the laser writing. This software can read in which state is each device so, for avoiding overexposure to laser radiation, shutter is controlled anytime, and future programs must have a line with this issue. Further external elements connections, like the optical beam shutter, must be connected to the Z-axis driver one and, the three stage axes are connected themselves by optical ports in series, for enabling a fast internal communication among them.

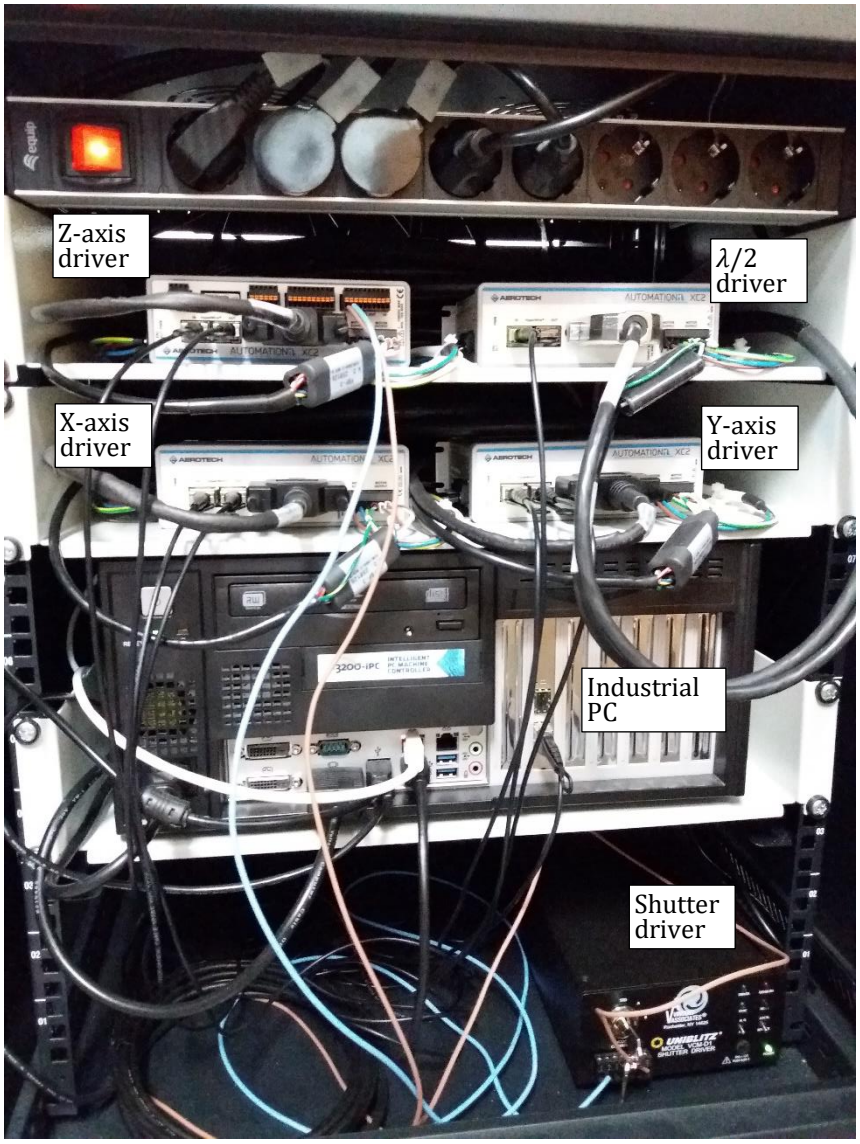

Figure A-9. Developed automation control system consisting of PC, four drivers, two power supplies (48V and 24V), plus an optical shutter driver, all mounted inside a single rack.

A.1.5 Sample preparation. First samples.

Once a sample is irradiated with the ultrashort pulse laser, pores must be polished to achieve a good optical quality. A picture of this maching employed is presented in Fig. A-10. After that, pores must be emptied for having air instead, using a wet etching process. This is achieved using phosphoric acid which

attacks photosensitized regions. This setup is shown in Fig. A-11 and. Finally, the first finished written pores are seen in Fig. A-12, concluding that the first results are very promising.

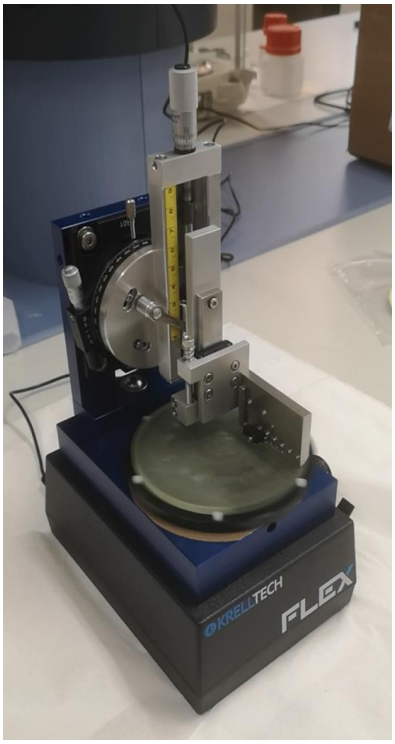

Figure A-10. Polishing of laser-processed samples to optical quality. After this polishing step, a wet etching process is performed.

Figure A-11. Ultrasound sonicator for etching.

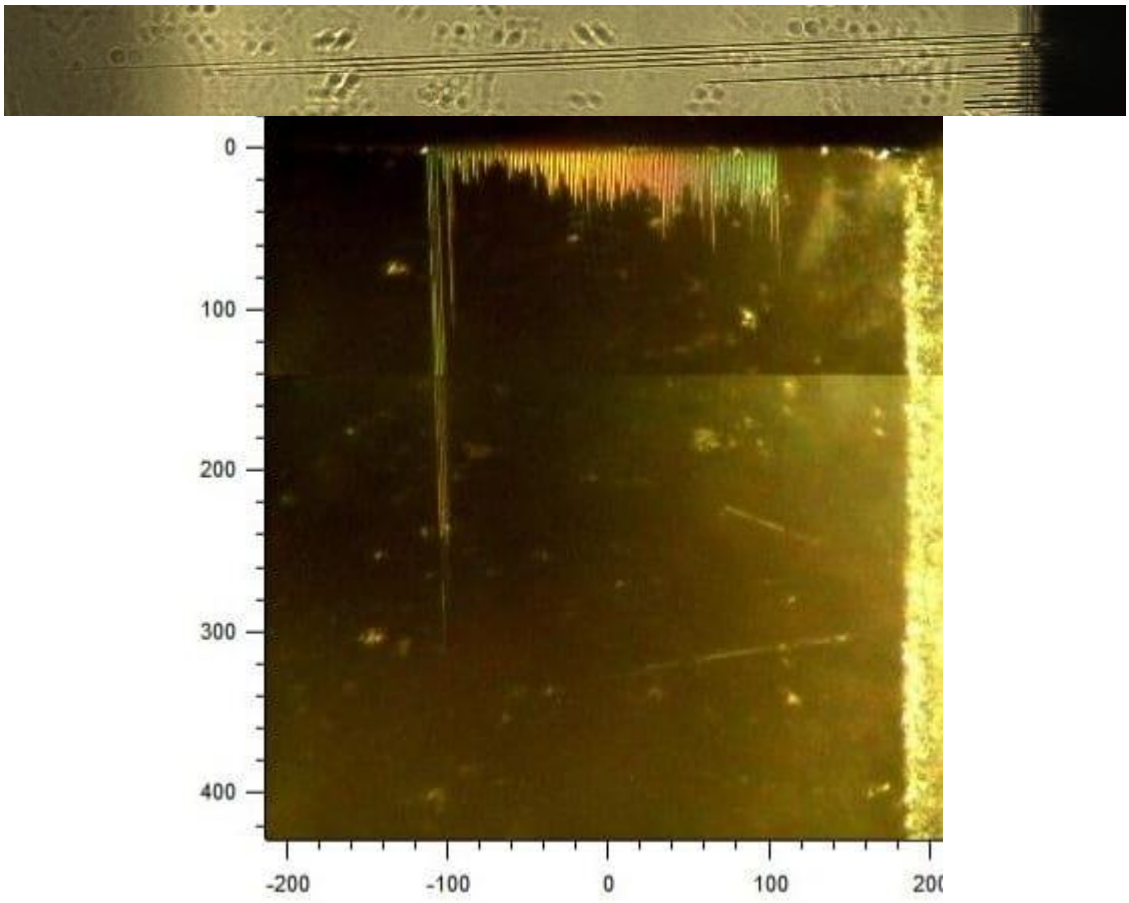

Figure A-12. First writing patterns in a YAG sample (below picture, units are in µm).

A.2 References

[Aerotech 2018] Aerotech (2018). *Data sheets.*

[Eksma 2020] EKSMA Optics (2020). *Ultrafast Pulse Picking Systems.* Version 20201001.

[Hetch 1998] Hetch E. (1998). *Óptica.* Addison Wesley.

[Lyons 2017] Lyons W. (2017). *Tutorial - Period, Frequency, and Duty Cycle - just over a minute!* [Video]. YouTube.

[Ophir 2021] Ophir (2021). *12A-v1 Data sheet.*

[Spectra 2002] Spectra-Physics (2002). *Tsunami Mode-Locked Ti:sapphire Laser.*

[Thorlabs(OC) 2021] Thorlabs (2021). *Optical Coatings.*

[Uhlig 2015] Uhlig S. (2015). *Self-Organized Surface Structures with Ultrafast White-Light: First Investigation of LIPSS with Supercontinuum.* BestMasters.